www.lpr-journal.org

LASER & PHOTONICS REVIEWS

WILEY-VCH

REPRINT

LASER
& PHOTONICS
REVIEWS

Laser Photonics Rev. **8,** No. 6, 882–888 (2014) / **DOI** 10.1002/lpor.201400043

ORIGINAL
PAPER

Abstract Micronanofabrication technologies developed so far pursue faithful conversion from digital models to matter structures. This is vital for microdevices in optics, mechanics, and electronics, where device shape and size matter. However, biotissues grow under rich environmental factor interactions, as demands novel manufacturing approaches for biomimetic and biological fabrication. Here, a concept of dynamic laser prototyping is reported, which is based on a new finding of a multilayered three-dimensional (3D) wrinkling phenomenon. The 3D wrinkling started with formation of a photocrosslinked hydrogel sheet by femtosecond laser direct writing. It was followed by spontaneous self-bending of the sheet, caused by a purposely designed sheet–substrate stress mismatch. The flower blooming process has been successfully mimicked, indicating broader usages of the technology in biotissue-growth-related manufacturing.

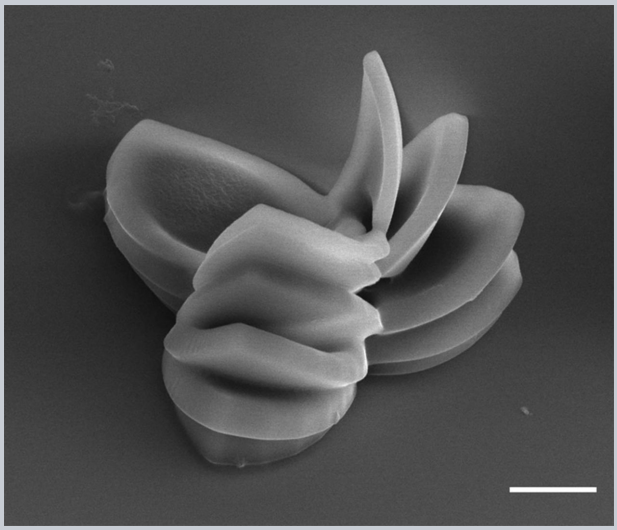

Dynamic laser prototyping for biomimetic nanofabrication

Dong-Xu Liu[1], Yun-Lu Sun[1], Wen-Fei Dong[1,*], Rui-Zhu Yang[1], Qi-Dai Chen[1], and Hong-Bo Sun[1,2,*]

1. Introduction

Lamellate wrinkle architectures are ubiquitous in nature, for example, in living tissues such as stems of plants like cabbage, onion and garlic, and in flower blooming. The highly complex three-dimensional (3D) structures were formed spontaneously by the cooperative interplay between the morphological instability induced surface wrinkles and self-organization of biological materials [1–6]. Great research efforts have been placed on fabrication of the hierarchical microstructures with the aim of their broad applications in areas as diverse as biomaterials, robotics, microfluidic devices, soft electronics and tunable photonics [7–10]. Corresponding micronanoprocessing technologies that involve usage of self-assembly, imprinting, molding, lithography, and direct laser writing were therefore developed to reach the end of biomimetic and biological fabrication [11–17]. However, mimicking the lamellate growth remains technically challenging since the current bionic manufacturing stays at the level of static prototyping [18–22]. In another words, faithful conversion from ready digital models to matter structures is pursued, but growth-accompanied complicated ambient effects including exerted forces are all ignored.

Here, we report a novel approach, dynamic laser prototyping (DLP) for biomimetic and biological nanofabrication, which is initiated from a new finding of a multilayered wrinkling phenomenon. The 3D wrinkling started with formation of a photocrosslinked hydrogel sheet by femtosecond laser direct writing (FsLDW). It was followed with spontaneous self-bending of the sheet, caused by a purposely designed sheet–substrate stress mismatch. Continuous laser scanning in the same position created new layers beneath the early bent sheets. They underwent similar bending, resulting ultimately in a complex 3D lamellate biomimetic structures. In the course of DLP, the laser scanning offers only an initial shape, while formation of the resultant structures needs assembly of partly or entirely created parts under an additional external force field. It is the cooperative interplay between the pinpoint laser prototyping and 3D wrinkling self-assembly, that makes dynamic laser prototyping a new concept.

2. Experimental materials and methods

Laser fabrication: Hydrogel microstructures were fabricated by a home-made FsLDW system, which is composed

[1] State Key Laboratory on Integrated Optoelectronics, College of Electronic Science and Engineering, Jilin University, 2699 Qianjin Street, Changchun, 130012, China
[2] College of Physics, Jilin University, 119 Jiefang Road, Changchun, 130023, China
*Corresponding author(s): Tel & Fax: +86 431 85168281; e-mail: wenfeidong@126.com, hbsun@jlu.edu.cn

of a femtosecond laser (Spectra Physics 3960-X1BB), a piezostage with the movement precision of 1 nm (Physik Instrumente P-622.ZCD), and a set of two galvano mirrors. The laser beam, delivering femtosecond pulses of 120 fs at 80 MHz repetition rate and 780 nm central wavelength, was tightly focused by a high-numerical-aperture (NA = 1.35) oil-immersion objective lens (60×). In order to avoid solution evaporation, a small chamber is used during the fabrication. The vertical resolution of the laser fabrication is around 1 mm depending on the laser power (relative to the photopolymerization threshold). In order to precisely control the sheet thickness, a vertical scanning step of 100 nm was adopted in the current research, meaning that the thickness of the sheet increases with 100 nm steps following each layer scanning. Smaller steps may be utilized, but the fabrication efficiency may be reduced, while larger steps may lead to the connection problem between vertical layers.

Materials: poly (ethylene glycol) (575) diacrylate (PEG-DA 575), acrylic acid (AAc), methylene blue (MB) were purchased from Sigma-Aldrich. All the chemicals were used as received. A water-responsive hydrogel prepolymer solutions (i.e. 62.5% PEG-DA 575, 12.5% AAc, 0.075% MB by weight in deionized water) were sonicated in the dark for ∼5 min in a 25 °C water bath to assure dissolution of all the chemicals and were used immediately. Prior to photopolymerization, coverslips were cleaned carefully by acetone, alcohol and deionized water for 15 min, respectively, and then dried before using.

Hydrogel polymerization: In order to minimize the effect of the evaporation during the fabrication, the hydrogel prepolymer solution had to be placed in a small chamber. Then, the femtosecond laser beam was focused into the solution and initiated the polymerization. Furthermore, the average laser power was measured at the back aperture of the focusing objective. After fabrication, all hydrogel samples were rinsed by deionized water for 5 times, each for 15 min, leading to complete removal of unpolymerized hydrogel, and then they were stored under room conditions for air drying. Generally 4 h would be long enough for further SEM characterization.

Characterization: *A) Scanning electron microscopy (SEM)*: Micronanoarchitectures were examined with a high-resolution LEO 1550 FEG SEM at the same acceleration voltages. The nominal thickness of a sputter coated Au film is 10–20 nm. *B) Optical microscopy*: Optical images and movies during fabrication were captured using the CCD camera (DV100, 10Moons) of the homemade FsLDW system. Optical microscopy characterization was carried out by an upright optical microscope (Motic BA400), equipped with 20×/0.25 and LPL40×/0.60 objective lenses.

3. Results and discussions

3.1. Design of stress mismatch reinforce mechanism

For dynamic laser prototyping mimick of lamellate growth (Fig. 1a), formation of self-bent sheets is a prerequisite. A self-bending phenomenon [1–3] is commonly observed in hydrogels because they suffer from morphological instabilities and large deformation owing to the low elastic modulus or high sensitivity to external stimuli [23, 24]. A PEG-DA

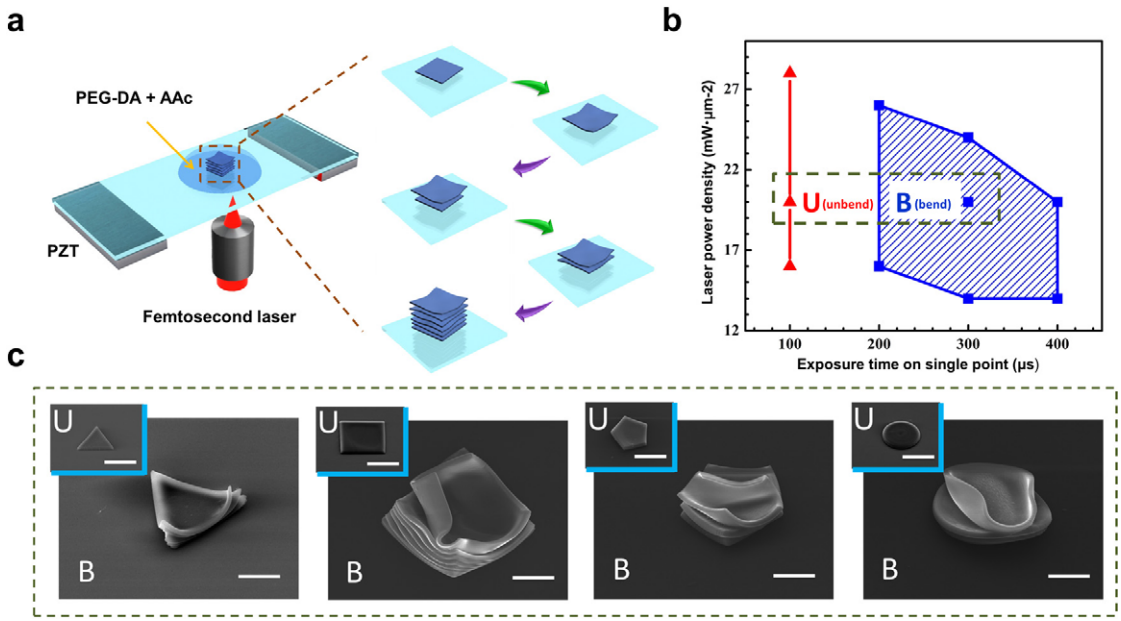

Figure 1 (a) Schematic of the technical sequence. (b) The $\tau - p$ map that locates the parameter sets (laser power density and exposure time on single point) for the occurrence of self-bending under a fixed hydrogen sheet thickness of 4 μm. The letter B denotes the bending occurrence and U means unbend. (c) SEM images of 4-mm thick and 25-μm circumcircle diameter sheets of different shapes. Scale bar: 40 μm for inset images and 20 μm for outset images.

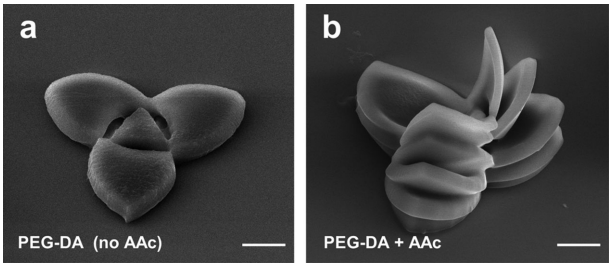

Figure 2 Materials aspect for dynamic versus static prototypings. (a) SEM image of 3D PEGDA hydrogel cuboid microstructure as the example of prototyping from a static model. (b) SEM image of a 3D bent structure enabled by the dynamic mimick, for which PEGDA/AAc hydrogel was pinpoint exposed by femtosecond laser direct wring in two dimensions. Scale bar: 20 μm.

based hydrogel was chosen in this research because of its intrinsic feature of easy photocrosslinking and excellent biocompatibility [25]. PEGDA was readily prototyped according to preprogrammed computer-aided design (CAD) models by FsLDW into structures of various geometries including those in three dimensions, and excellent morphology and integrity of microstructures were attainable (Fig. 2a, Supplementary Fig. S1). However, it is difficult for a thus-polymerized thin layer to self-bend or wrinkle from a rigid substrate due to the relatively strong adhesion (Supplementary Fig. 3a, Mov. 1). An appropriate mechanism should be provided to reinforce the stress mismatch between the polymer layer and substrate, for which a second functional monomer of acrylic acid (AAc) was added. The AAc is the simplest unsaturated carboxylic acid, consisting of a vinyl group connected directly to a carboxylic acid terminus. It exhibits superabsorbency to water molecules when they combine with themselves to form a polyacrylic acid block, or with other monomers, here PEDGA, by reacting at their double bond, and formed copolymers. Water molecules are rapidly drawn into and held tightly inside the polymer network by hydrogen bonding (Supplementary Fig. S2). The water-retention capacity of some specially designed superabsorbent polymers may be hundreds of times their weight, resulting in great volume expansion. Here, when a PEGDA-AAC thin film is prototyped onto a rigid substrate, the expansion-induced stress mismatch may drive it to peel off. Movement of the released parts towards free space causes the sheet to curl up.

3.2. DLP: dynamic laser prototyping

The resulted precursory mixture consisted therefore of PEGDA, AAc and MB as the photoinitiator. It was prototyped into various shapes by FsLDW that was conducted with a home-made system (Figs. 1a and c). The best fabrication resolution is found to be better than 530 nm (Supplementary Fig. S4). The pinpoint laser-scanning induced local polymerization of monomers, in the meantime, the earlier-created polymer network started to absorb water molecules from the ambient aqueous solution. The size expansion of a square sheet is slightly visible in the course of laser writing, and part of or an entire sheet was dramatically stripped from the substrate when a threshold is reached (Supplementary Mov. 2). From the movie, the rate of volume expansion was estimated to be nearly 200% even if the film thickness is as small as 4 μm. It is therefore evident that the nature of dynamic laser prototyping is, involving interactions of ambient factors in the process of complex structure formation, not just prototyping a pattern according to a ready static CAD model [19, 20, 26, 27]. Compared with the local force provided by bond formation during photopolymerization, the stress field interacting on the entire sheet provides a global force, which works as the external field that coupled to the fabrication process. The coupling makes it feasible to dynamically mimic some tissue growing processes such as lamellate growth in flower blooming. In Fig. 2b, all the multilayered flower petals were fulfilled by laser prototyping in the same position in two dimensions. Upon completion of a layer scanning, it was spontaneously bent up from the substrate (Supplementary Mov. 3). The water molecules absorbance by the polymer network, the petal volume expansion (swelling), and the stress-mismatch-induced wrinkling of the polymerized thin layers took place in the course of laser scanning. It is the mutual interactions of these factors that enabled the DLP concept, as well as mimicking of the lamellate growth.

3.3. Tailoring morphology and crosslinking density

The surface morphology of polymerized structures was sensitively affected by both the precursory materials composition and the laser processing conditions. The latter includes the laser power density (p) and the single-point exposure time (τ). Experimentally, the concentrations of AAc+PEGDA and the photoinitiator MB in the aqueous solution were optimized to 75% w/w and 0.075% w/w, respectively. According to the resulting photopolymerization thresholds, the laser power density and the scanning step were selected to $p = 20$ mW $\cdot$ μm^{-2} (Supplementary Fig. S3) and 100 nm. The effect of concentration ratio of AAc relative to PEGDA on the surface quality was investigated. Adjusting AAc: PEGDA from 5:1, 4:2, 3:3, 2:4 to 1:5 at the fixed monomers concentration of 75%w/w, we found that protrusions tended to be less sharp and the surface of the hydrogel sheet became smoother (Fig. S5). This could be reasonably ascribed to a lessened phase separation of polyacrylic acid block from the polymer network, as set by the upper limit of AAc concentration to 12.5%w/w in the entire precursory solution or AAc:PEGDA = 1:5 considering both the requirements of stress mismatch and morphology.

In addition to AAc concentration, the density of crosslinking nodes in a polymer network is another important factor that affects the mechanical strength of polymerized sheet. Generally speaking a loosened network

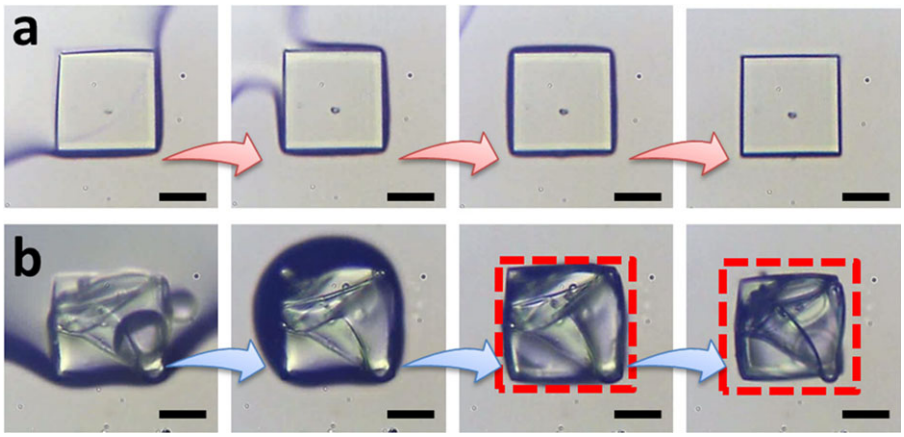

Figure 3 (a) Screenshot of the Supplementary Mov. 1. The microstructure fabricated by pure PEG-DA is immersed in a droplet of water. With water evaporation, the volume of the microstructure is nearly unchanged. (b) The same process for the microstructure fabricated by PEG-DA and AAc and its volume changed about 25%. The arrows indicate from left to right different stages of water evaporation. Scale bar: 20 μm.

provides more space for water molecules. However, here the AAc concentration in the entire network is relatively low (AAc:PEGDA = 1:5), implying that the higher the degree of polymerization is, the higher the density of AAc molecules that are included, and correspondingly the higher the water-absorption capability and the larger expansion force would be realized. The expansion-induced stress mismatch determines whether a polymerized sheet was bent or stayed adhered to the substrate. The degree of polymerization for a given material is a function of laser power density and single-point exposure duration, but not simply their product (τp) as in the case of linear exposure, because in general laser scanning does not induce complete polymerization and crosslinking of monomer molecules. Aτ-p mapping revealed that a closed area, the shadow region (Fig. 1b) denoted by letter B (bend), existed, which is appropriate for the occurrence of sheets bending. Outside of the region, denoted by letter U (unbend), no sheet was bent either because either of insufficient AAc incorporation into the polymer network (left and lower region) or of material breakdown (right and upper region). The location of region B in the τ-p coordinate system is hardly affected by the sheet shape no matter whether they are a triangle, rectangle, pentagon or a circle for a given contact area and layer thickness. In Fig. 1c, all patterns possess a circumcircle diameter of 25 μm and a height of 4 μm. When the exposure time is $\tau > 100$ μs, lamellate wrinkling took place, while $\tau < 100$ μs led to solely even surface structures.

3.4. Mimicking lamellate growth in flower blooming by DLP

Located by the map in Fig. 1b, a wide range of laser parameter sets could be adopted for producing self-bent sheets. If a second layer was in situ scanned at the same position after earlier-created sheets were bent, multilayered structures were finally attained (Fig. 4). The entire bending-accompanied flower blooming process has been recorded by optical microscopic images (Figs. 4a–f and Supplementary Mov. 3). Here the FsLDW served as the dynamic source of lamellate growth by creating initial

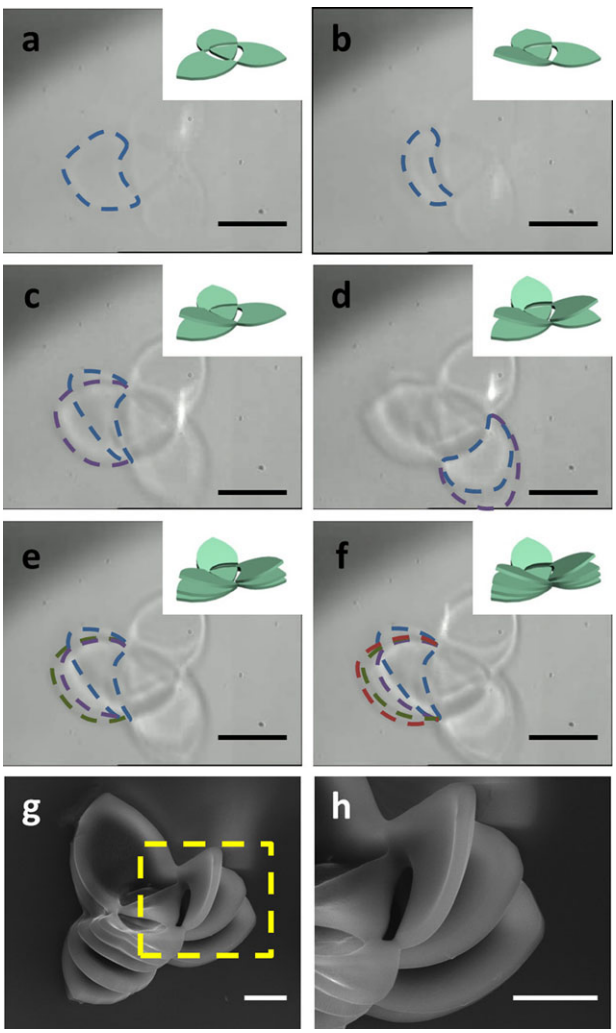

Figure 4 (a–f) Screenshot images captured by a real-time monitoring charge-coupled device (CCD) camera, exhibiting "flower" blooming. The top-right insets the model design and dotted lines of different colors represent different layers. Scale bar: 20 μm. (g and h) SEM images of self-bent structure, a bloomed flower and its local magnification. Scale bar: 10 μm.

sheet shapes and continuously adding new materials to it through repeated laser scanning (Fig. 4a). The vertical position of the laser beam did not change and it moved solely along the X–Y direction, by which planar patterns such as a 3-petal flower (Figs. 4g and h) were prepared. When the film thickness reached a certain value, one of the petals started to be self-bent (Fig. 4b). When the accumulated mismatching stress approached the detachment threshold, even one more scanning run led to spontaneously lifting up of all petals. In Figs. 4g and h, the petal length was originally designed to be 50 μm and the height (the sheet thickness) was 4 μm. After blooming, the petal rose to a height of 30 μm, in the meantime, the lateral petal size expanded, too.

3.5. The stress field as the external field coupled to the fabrication process

The bending threshold was investigated with purposely designed experiments by varying the sheet shape (Figs. 1b and c), the thickness (Fig. 5b) and their size (Fig. 5c). It was found that the occurrence of the self-bending is almost independent of the shape as pointed out earlier, and slowly affected by the size (contact area). For example, for a fixed layer thickness of $t = 4$ μm, bending takes place only when the side length of a square is larger than 40 μm (Fig. 5c). It is not surprising that the bending is quite sensitive to the layer thickness, and its variation at a 1% level determined whether a sheet (see earlier examples in Fig. 4) stayed attached or bent. An underlying reason is the inhomogeneous distribution of stress in the vertical direction. The early polymerized lower portion of a sheet absorbed more water molecules and more expanded. That is why the petals bent upwards.

The distribution of the mismatching stress was considered as the external field, stress field, to couple to the fabrication process in the current DLP. It is interesting to know from the field analysis how the bending is initiated. Since the lamellate growth is a process that increases thickness, a stress field model was established to predict the relationship between the thickness and the self-bending (Fig. 6). It was assumed that a square hydrogel sheet was an isotropic elastic layer that obeyed Hooke's law under stress. The layer was restricted only in the bottom portion and was free in other dimensions. It underwent a 2D homogeneous swelling by absorbing water. The stress–strain relation follows the relation,

$$\begin{cases} \varepsilon_x = \dfrac{1}{E}\left[\sigma_x - \nu\left(\sigma_y + \sigma_z\right)\right] \\ \varepsilon_y = \dfrac{1}{E}\left[\sigma_y - \nu\left(\sigma_z + \sigma_x\right)\right] \\ \varepsilon_z = \dfrac{1}{E}\left[\sigma_z - \nu\left(\sigma_x + \sigma_y\right)\right] \end{cases}, \qquad (1)$$

where ε is the strain, E is the elastic modulus, σ is the stress, ν is Poisson's ratio, the subscripts x, y and z correspond to

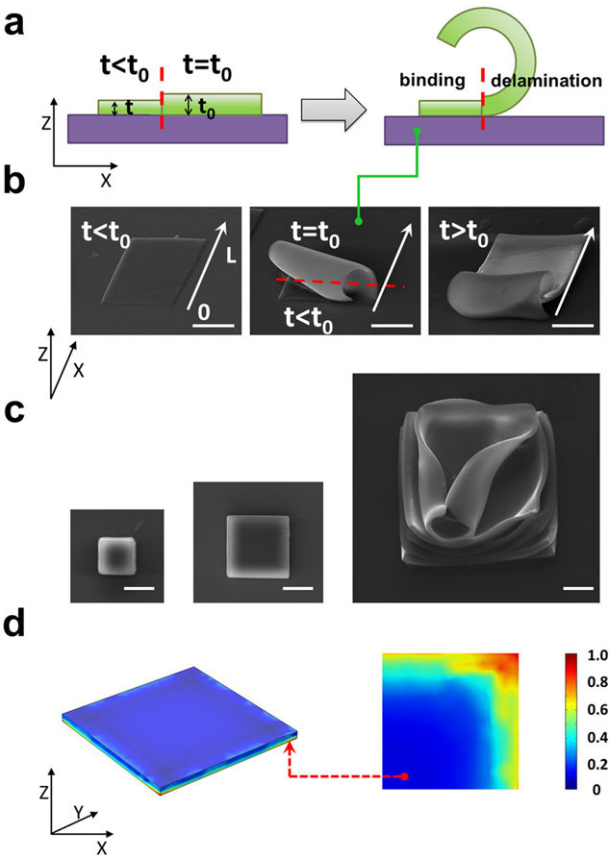

Figure 5 (a) Illustration of the effect of the critical thickness (t_0) for occurrence of self-bending, and (b) experimental evidence of the existence of t_0. When the sheet is thinner, wrinkling does not occur because not enough stress could be accumulated to balance the adhesion force. However, this can occur if they are thicker. Scale bar: 20 μm. (c) The size effect for the self-bending behaviors. The thickness for all sheets were fixed to 4 μm. Scale bar: 10 μm. (d) Color map of the distribution of the stress caused by the total stress mismatch, which was calculated by the FEM simulation. The right image is a zoom-in view at the vertices on the sheet bottom, indicating why bending takes place preferentially there.

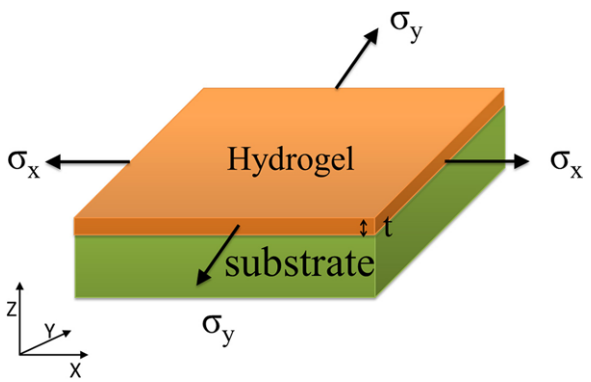

Figure 6 Schematic of the stress field model used for the force analysis and FEM calculation.

the *X*-axis, *Y*-axis and *Z*-axis directions. In a single hydrogel layer, the *Z*-axis is stress free and $\varepsilon_x = \varepsilon_y$, so the inplane stress is

$$\sigma_x = \sigma_y = \frac{E_f}{1-\nu_f}\varepsilon_f = \sigma_f, \tag{2}$$

where ε_f and σ_f are the strain and the stress in the layer, E_f and ν_f are the elastic modulus and the Poisson's ratio of the single hydrogel layer. For the homogeneous material the mismatch strain is

$$\varepsilon_x = \varepsilon_y = \frac{\Delta L}{L} = \varepsilon_f, \tag{3}$$

where L is the side length, ΔL is the difference of the length after and before the swelling. Integrating Eqs. (2) and (3), we get the energy of the strain in a unit thickness of the layer

$$E_S^{'} = \frac{1}{2}\sigma_f\varepsilon_f = \frac{E_f}{2(1-\nu_f)}\left(\frac{\Delta L}{L}\right)^2. \tag{4}$$

For a certain layer, the values of E_f, ν_f, ΔL and L are constants, so the E_S is also a constant. If the total energy of the strain (E_S) in the layer caused by the stress mismatch is larger than the binding energy (E_B) by the substrate, bending occurs. The bending condition is,

$$E_S = \int_0^t E_S' d_z \geq E_B, \tag{5}$$

where t is the thickness of the layer in the *Z*-axis direction. The inequality condition is preferentially satisfied under actual experimental conditions at a certain position, generally the corners of a sheet, by minor disturbances to the planarly uniform distribution of the mismatching stress.The stress field could be further manifested from a finite element method (FEM) calculation. Given a mismatch strain of 25% (Fig. 3b) a Young's modulus of 183 MPa, and a Poisson's ratio [5] of 0.4, the 3D stress distribution is shown in Fig. 5d. The rainbow bar gives the normalized force intensity in the stress field by different colours. The compressive stress was concentrated on the bottom surface, sides and vertexes. That is, the bending condition was preferentially satisfied at the bottom corner positions, which is the location at which bending was initiated.

FEM simulations were performed by COMSOL Multiphysics 4.2 using the standard solid mechanics module as the "Add Physics". The mechanical performance of the sheet including Young's modulus (183 MPa) was measured from macroscale sheets of the same composition. Then, we assumed it was the same as the microscale case. The Poisson's ratio was attained from the literature [5], where the value is around 0.4 for most hydrogel materials. The tensile stress is calculated by the change of the rectangular surface areas before and after its release from the substrate (25% according to Fig. 3b). Based on these parameters, the strain between the top side of a sheet (free side) and bottom side (bond to the substrate) under a certain thickness was calculated.

The study type was selected as stationary. The geometry length unit was set to μm. The geometry shape was built as a block with width, depth and height of 40, 40 and 4. A mismatch strain of 25% in the *x*–*y* plane as mentioned above was given as the initial strain in the linear elastic material model. With building mesh with extra fine element size, a 3D stress distribution was obtained as shown in Fig. 5d. The rainbow bar gives the normalized force intensity in the stress field by different colors.

4. Conclusion and outlook

The current micronanofabrication technologies including 3D printing technologies emphasize faithful conversion of a CAD model to matter structures. This is indispensable for production of micromechanical, microelectric, and micro-optical components where precise shape and size matter. In these fabrications, environmental factors such as polymerization-induced volume shrinkage, the volume expansion, and fluidity of the precursory solution, and temperature gradient are all considered as negative factors to eliminate. However, for some biomimetic or biological fabrications, solely accurate size and shape prototyping is insufficient since the development of real-world tissues is not only a result of material addition, but a process of interactions between grown parts, or between the created structures and environments. In another words, the structures are alive, and the fabrication process itself matters. From this point of view, a micronanoprocessing technology that positively involves interactions of environmental factors is necessary. To reach this end, we proposed the new concept of dynamic laser prototyping based on a multilayered wrinkling phenomenon. The fundamental principle is combination of (i) creation of the planar gel sheet by direct laser writing and (ii) self-bending of the sheets subject to the stress-mismatched-induced bending force. By this means, the dynamic process of a flower blooming was successfully mimicked.

Environmental factors that could be further induced in the fabrication process include thermal, electronic, magnetic, optical, and even biochemical stimuli in addition to the mismatching stress field. The DLP fabrication itself is actually an external-field coupling process. The merit of FsLDW was adopted in the external-field coupling micronanofabrication lies at least in four aspects: (a) the minimal intrusion of material addition to the ready parts since the laser is transparent and the material provision is prompt and sufficient (Fig. 1a, and Supplementary Mov. 2), as compared with the general prototyping technologies like 3D printing; (b) the laser prototyping process itself is basically immune to the disturbance of the coupling of an external field. It is seen that FsLDW proceeds properly with the exerted stress field (Supplementary Mov. 2 and 3); (c) wide range of possibilities to tune fabrication/growth speed, to accommodate effects taken by the environment

factors. This capability is important since the external field coupling may effect from very fast (e.g., electrically, magnetically) to very slow (thermally or biochemically); Although not discussed in detail, it is not surprising to notice that various thresholds are affected by scanning speed, and the 4 μm thickness is always to be finished when bending occurs (Figs. 5a–c, and Supplementary Mov. 2 and 3); (d) FsLDW provides best available 3D resolution, which would be needed for growth simulation of more complicated biotissues. The linewidth achieved with the current materials is 570 nm (Fig. S4), much smaller than general cell sizes. It is the real-time multifield coupling that makes the laser prototyping dynamic, and conversely, FsLDW is best suited to the requirement of field coupling.

Acknowledgements. The authors gratefully acknowledge support from the National Basic Research Program of China (973 Program) (Grant Nos. 2011CB013003 and 2014CB921302) and from National Science Foundation of China (Grants Nos. 61137001, 61127010, and 51335008).

Supporting Information: for this article is available free of charge under http://dx.doi.org/10.1002/lpor.201400043

Received: 22 February 2014, **Revised:** 4 June 2014, **Accepted:** 18 June 2014

Published online: 16 July 2014

Key words: Laser prototyping, femtosecond laser, nanofabrication, lamellate growth, surface wrinkling.

References

[1] B. Li, Y. P. Cao, X. Q. Feng, and H. J. Gao, Soft Matter **8**, 5728–5745 (2012).
[2] L. Ionov, Macromol. Chem. Phys. **214**, 1178–1183 (2013).
[3] L. Ionov, J. Mater. Chem. **22**, 19366–19375 (2012).
[4] J. Genzer and J. Groenewold, Soft Matter **2**, 310–323 (2006).
[5] J. Yin, J. L. Yagüe, D. Eggenspieler, K. K. Gleason, and M. C. Boyce, Adv. Mater. **24**, 5441–5446 (2012).
[6] J. Y. Chung, A. J. Nolte, and C. M. Stafford, Adv. Mater. **23**, 349–368 (2011).
[7] H. Kim and S. Kwon, Science **339**, 150–151 (2013).
[8] E. Munch, M. E. Launey, D. H. Alsem, E. Saiz, A. P. Tomsia, and R. O. Ritchie, Science **322**, 1516–1520 (2008).
[9] D. Y. Khang, J. A. Rogers, and H. H. Lee, Adv. Funct. Mater. **19**, 1526–1536 (2009).
[10] J. A. Rogers, T. Someya, and Y. Huang, Science **327**, 1603–1607 (2010).
[11] K. Osada, H. Cabral, Y. Mochida, S. Lee, K. Nagata, T. Matsuura, M. Yamamoto, Y. Anraku, A. Kishimura, N. Nishiyama, and K. Kataoka, J. Am. Chem. Soc. **134**, 13172–13175 (2012).
[12] E. Donath, G. B. Sukhorukov, F. Caruso, S. A. Davis, and H. Möhwald, Angew. Chem. Int. Ed. **37**, 2201–2205 (1998).
[13] D. Wu, Q. D. Chen, B. B. Xu, J. Jiao, Y. Xu, H. Xia, and H. B. Sun, Appl. Phys. Lett. **95**, 091902 (2009).
[14] S. H. Park, D. Y. Yang, and K. S. Lee, Laser Photon. Rev. **3**, 1–11 (2009).
[15] E. T. Ritschdorff, R. Nielson, and J. B. Shear, LabChip **12**, 867–871 (2012).
[16] L. T. Romankiw, Electrochimica Acta **42**, 2985–3005 (1997).
[17] B. Kaehr and J. B. Shear, J. Am. Chem. Soc. **129**, 1904–1905 (2007).
[18] C. N. LaFratta, J. T. Fourkas, T. Baldacchini, and R. A. Farrer, Angew. Chem. Int. Ed. **46**, 6238–6258 (2007).
[19] Y. L. Zhang, Q. D. Chen, H. Xia, and H. B. Sun, Nano Today **5**, 435–448 (2010).
[20] H. Xia, J. Wang, Y. Tian, Q. D. Chen, X. B. Du, Y. L. Zhang, Y. He, and H. B. Sun, Adv. Mater. **22**, 3204–3207 (2010).
[21] K. S. Lee, D. Y. Yang, S. H. Park, and R. H. Kim, Polym. Adv. Technol. **17**, 72–82 (2006).
[22] S. Rekštytė, M. Malinauskas, and S. Juodkazis, Opt. Exp. **21**, 17028–17041 (2013).
[23] Z. B. Hu, Y. Y. Chen, C. J. Wang, Y. D. Zheng, and Y. Li, Nature **393**, 149–152 (1998).
[24] Y. Tokudome, K. Suzuki, T. Kitanaga, and M. Takahashi, Sci. Rep. **2**, 1–6 (2012).
[25] L. D. Zarzar, P. Kim, M. Kolle, C. J. Brinker, J. Aizenberg, and B. Kaehr, Angew. Chem. Int. Ed. **50**, 9356–9360 (2011).
[26] Y. L. Sun, W. F. Dong, R. Z. Yang, X. Meng, L. Zhang, Q. D. Chen, and H. B. Sun, Angew. Chem. Int. Ed. **51**, 1558–1562 (2012).
[27] Y. L. Sun, D. X. Liu, W. F. Dong, Q. D. Chen, and H. B. Sun, Opt. Lett. **37**, 2973–2975 (2012).